A New $K-\varepsilon$ Turbulence Parameterization for Mesoscale Meteorological Models

ANDREA ZONATO,[a] ALBERTO MARTILLI,[b] PEDRO A. JIMENEZ,[c] JIMY DUDHIA,[c] DINO ZARDI,[a]
AND LORENZO GIOVANNINI[a]

[a] *Atmospheric Physics Group, Department of Civil, Environmental and Mechanical Engineering, University of Trento, Trento, Italy*
[b] *Center for Energy, Environment and Technology (CIEMAT), Madrid, Spain*
[c] *National Center for Atmospheric Research, Boulder, Colorado*

ABSTRACT: A new one-dimensional 1.5-order planetary boundary layer (PBL) scheme, based on the $K-\varepsilon$ turbulence closure applied to the Reynolds-averaged Navier–Stokes (RANS) equations, is developed and implemented within the Weather Research and Forecasting (WRF) Model. The new scheme includes an analytic solution of the coupled equations for turbulent kinetic energy and dissipation rate. Different versions of the PBL scheme are proposed, with increasing levels of complexity, including a model for the calculation of the Prandtl number, a correction to the dissipation rate equation, and a prognostic equation for the temperature variance. Five different idealized cases are tested: four of them explore convective conditions, and they differ in initial thermal stratification and terrain complexity, while one simulates the very stable boundary layer case known as GABLS. For each case study, an ensemble of different large-eddy simulations (LES) is taken as reference for the comparison with the novel PBL schemes and other state-of-the-art 1- and 1.5-order turbulence closures. Results show that the new PBL $K-\varepsilon$ scheme brings improvements in all the cases tested in this study. Specifically, the more significant are obtained with the turbulence closure including a prognostic equation for the temperature variance. Moreover, the largest benefits are obtained for the idealized cases simulating a typical thermal circulation within a two-dimensional valley. This suggests that the use of prognostic equations for dissipation rate and temperature variance, which take into account their transport and history, is particularly important with the increasing complexity of PBL dynamics.

KEYWORDS: Boundary layer; Mesoscale models; Parameterization

1. Introduction

One of the primary sources of uncertainty in mesoscale numerical weather prediction (NWP) models is the representation of thermodynamic processes in the planetary boundary layer (PBL) (Cohen et al. 2015; Nielsen-Gammon et al. 2010). These processes are strongly influenced by the mechanical and thermal mixing induced by Earth's surface, which is associated with turbulent eddies. The spatiotemporal scales of such eddies cannot be explicitly resolved at the grid scales and time steps typical of NWP models at the mesoscale (Stull 1988). For this reason, PBL parameterization schemes in the framework on the Reynolds-averaged Navier–Stokes (RANS) equations are employed at the typical resolution of mesoscale models, ranging from hundreds of meters to some kilometers, to parameterize the vertical turbulent flux of momentum, heat, and moisture.

PBL schemes can be divided into two main categories (Zhang et al. 2020): the eddy-diffusivity mass-flux (EDMF) approach and the traditional eddy-diffusivity (K-theory) parameterizations. The EDMF approach consists in the combination of the K-theory closure, which parameterizes the turbulent transport by small eddies, with the mass flux component accounting for nonlocal organized eddy fluxes (Angevine et al. 2010; Han et al. 2016; Olson et al. 2019). On the other hand, K-theory turbulence closures can be classified depending on the order

of the RANS equations that are resolved. The one-order turbulence closures estimate the eddy viscosity/diffusivity (ν_M, ν_H) based on the vertical wind shear and temperature stratification. One example is the well-known Yonsei State University scheme (YSU; Hong et al. 2006). The 1.5-order closures include a prognostic equation for the turbulent kinetic energy (TKE) and a turbulent mixing length scale (ℓ_K) for calculating vertical mixing coefficients ($K-\ell$ approach). The equation for TKE accounts for the contribution of buoyancy, shear, vertical transport, and dissipation rate (ε). The latter is assumed to be proportional to a dissipation mixing length (ℓ_ε), set equal to ℓ_K in the simplest 1.5-order turbulence closures. However, Bougeault and Lacarrere (1989) (hereafter BouLac) utilized two different length scales, depending on atmospheric stability.

An alternative approach to determine the TKE and the vertical mixing coefficients in 1.5-order (or higher) closures is to employ an additional prognostic equation for the dissipation rate, in order to avoid defining the diagnostic length scales. This kind of closure, called $K-\varepsilon$ hereafter, has been widely used to reproduce vertical PBL profiles in various conditions (Launder and Spalding 1974; Detering and Etling 1985; Duynkerke 1988; Langland and Liou 1996). Beljaars et al. (1987) compared $K-\ell$-based and $K-\varepsilon$-based schemes and found that the $K-\varepsilon$ better preserves the "memory effects" of the PBL, because the prognostic equation of ε, including its vertical transport, takes into account its distribution at the previous time step to calculate its temporal evolution, which is not considered in $K-\ell$ schemes. Wang (2001, 2002) implemented a $K-\varepsilon$ scheme in a tropical cyclone model, and later the model was used for regional climate studies, e.g., for investigating the

Asian summer monsoon rainfall (Wang et al. 2003; Souma and Wang 2009) and the eastern Pacific boundary layer clouds (Wang et al. 2004a,b; Xie et al. 2007). More recently, Zhang et al. (2020) incorporated the K–ε version of Wang (2001, 2002) in the Weather Research and Forecasting (WRF) Model (Skamarock et al. 2019). The new scheme was evaluated in the PBL topped by stratocumulus clouds over the southeast Pacific and the southern Great Plains, finding that the K–ε performed similarly to other state-of-the-art PBL schemes. However, several studies (Launder and Spalding 1983; Sukoriansky et al. 2005; Lazeroms et al. 2015; van der Laan et al. 2017; Zeng et al. 2020; Zeng and Wang 2020) highlighted the necessity to modify the standard K–ε turbulence closure, since it does not perform well in both convective and stable regimes, especially in flows with strong mean shear. Although Zhang et al. (2020) showed good performance of their K–ε scheme as mentioned above, recent insights have even shown that additional prognostic equations are required, in particular for the potential temperature variance (Mauritsen et al. 2007; Zilitinkevich et al. 2007, 2013).

This work shows the advantage of a new K–ε turbulence closure, with appropriate modifications, to face the aforementioned problems, to improve its capability of reproducing simple idealized cases when implemented in the WRF mesoscale model. Specifically, the standard K–ε closure is modified through (i) the estimation of the vertical profile of the Prandtl number as in Hong et al. (2006), to take into account the difference between eddy diffusivity and eddy viscosity, (ii) an additional correction term in the prognostic equation for the dissipation rate as in Zhang et al. (2020), to make the new closure consistent with the Monin–Obukhov similarity theory (MOST), (iii) the coupling with a prognostic equation for the turbulent potential energy (TPE; proportional to the temperature variance) as in Lazeroms et al. (2015) and Želi et al. (2019), to consider its effect on the turbulent heat flux. The latter, for convective cases, is also compared with a closure employing a nonlocal counter-gradient term, computed as in Ching et al. (2014). The novel PBL scheme is tested by means of idealized simulations. Idealized simulations include several flat terrain cases, with different thermal stratification in both convective and stable regimes, and a complex terrain case in convective conditions with various wind forcing. The aim is to assess if the employment of additional prognostic equations, considering "memory effects" and turbulent transport of the dissipation rate and temperature variance, is beneficial when reproducing PBL processes. The newly developed PBL scheme is validated against ensembles of large-eddy simulations (LES), taken as reference for each case study, and compared with state-of-the-art PBL schemes, at different orders, already implemented in WRF.

The paper is organized as follows: the theory of the newly introduced PBL scheme, along with the novel computational solution is presented in section 2. The setup of the five idealized case studies and the methodology for the calculation of the turbulent fluxes are described in section 3. In section 4 model outputs are compared with LES for each case study, and the performance of the various PBL schemes is quantified through statistical parameters. Finally, in section 5, results are summarized and discussed.

2. The model

The turbulence parameterization scheme presented here is developed in the framework of the RANS equations, in which each variable of the mean flow is decomposed into its mean, representing an ensemble average (uppercase letters), and fluctuating part (lowercase letters). Planetary boundary layer (PBL) parameterizations generally assume horizontal homogeneity, to consider only the vertical derivative of the turbulent fluxes. Then turbulent contribution to the mean flow dynamics is given by the following:

Zonal wind speed:

$$\frac{\partial U}{\partial t} = -\frac{\partial \overline{uw}}{\partial z}. \tag{1a}$$

Meridional wind speed:

$$\frac{\partial V}{\partial t} = -\frac{\partial \overline{vw}}{\partial z}. \tag{1b}$$

Potential temperature:

$$\frac{\partial \Theta}{\partial t} = -\frac{\partial \overline{w\theta}}{\partial z}. \tag{1c}$$

The quantities $\overline{wc}$, where $c = (u, v, \theta)$ represent the vertical turbulent fluxes. The aim of this work is to find a closure for these turbulent fluxes, in terms of mean velocity and mean potential temperature (and mean water vapor mixing ratio, but here we consider only dry atmosphere cases) that does not depend on a diagnostic length scale, but instead on the local properties of the atmospheric state, e.g., adopting a prognostic equation for the dissipation rate, skipping the step of defining a diagnostic length scale that depends on atmospheric conditions.

a. The standard K–ε turbulence closure

Similarly to most turbulence models, in the closure presented here the turbulent fluxes are parameterized, in analogy with molecular diffusion, as a function of an eddy viscosity/diffusivity and of the mean gradients:

$$\overline{uw} = -\nu_M \frac{\partial U}{\partial z}, \tag{2a}$$

$$\overline{vw} = -\nu_M \frac{\partial V}{\partial z}, \tag{2b}$$

$$\overline{w\theta} = -\nu_H \frac{\partial \Theta}{\partial z}, \tag{2c}$$

where ν_M is the eddy viscosity and ν_H the eddy diffusivity. To close Eq. (1), the eddy coefficients need to be parameterized. Moreover, in subsection c we will discuss an additional term for the turbulent heat flux, which takes into account the vertical transport by large eddies. A simple scaling analysis suggests

$$\nu_M, \nu_H \sim \ell_K K^{1/2}, \tag{3}$$

where ℓ_K is a mixing length scale, and $K = (\overline{u^2} + \overline{v^2} + \overline{w^2})/2$ is the turbulent kinetic energy per unit mass. The prognostic equation for K allows to take into account its history and transport effects and, considering again horizontal homogeneity and neglecting pressure fluctuations, is given by

$$\frac{\partial K}{\partial t} = -\frac{\partial \overline{wk}}{\partial z} - \overline{uw}\frac{\partial U}{\partial z} - \overline{vw}\frac{\partial V}{\partial z} + \frac{g}{\Theta_0}\overline{w\theta} - \varepsilon. \quad (4)$$

The terms on the right-hand side represent, respectively, the turbulent transport, the vertical shear production of both horizontal directions, the buoyancy production/destruction, and the dissipation rate. To close Eq. (4), in standard 1.5-order turbulence closures the dissipation rate ε is usually set dependent on K and a length scale ℓ_ε, in a way similar to Eq. (3):

$$\varepsilon \sim \frac{K^{3/2}}{\ell_\varepsilon}. \quad (5)$$

From Eqs. (5) and (3), one obtains

$$\nu_M = c_\mu \frac{K^2}{\varepsilon}, \quad (6a)$$

$$\nu_H = \frac{c_\mu}{\Pr} \frac{K^2}{\varepsilon}, \quad (6b)$$

where c_μ is a constant, usually set equal to 0.09 (Launder and Spalding 1983), and Pr is the turbulent Prandtl number.

On the other hand, in K–ε turbulence closures the dissipation rate ε is calculated through its prognostic equation:

$$\frac{\partial \varepsilon}{\partial t} = -\frac{1}{\sigma_\varepsilon}\frac{\partial \overline{\varepsilon w}}{\partial z} - \left[c_1\left(\overline{uw}\frac{\partial U}{\partial z} + \overline{vw}\frac{\partial V}{\partial z}\right) - c_3\frac{g}{\Theta_0}\overline{w\theta}\right]\frac{\varepsilon}{K}$$
$$- c_2\frac{\varepsilon^2}{K}, \quad (7)$$

where c_1, c_2, c_3, and σ_ε are set equal to 1.44, 1.92, 1.44, and 1.3, respectively (Launder and Spalding 1974). The terms on the right hand side represent, respectively, the turbulent transport, the shear production, the buoyancy production/destruction and the viscous dissipation.

In this work the Prandtl number in Eq. (6b) is computed as in Hong et al. (2006), depending on the height above the ground z, the PBL height h, and the state of the surface layer:

$$\Pr = 1 + (\Pr_0 - 1)\exp\left[\frac{-3(z - 0.1h)^2}{h^2}\right], \quad (8)$$

where $\Pr_0 = \phi_h/\phi_m + 0.68\nu_k$, calculated using the similarity functions ϕ_i evaluated at the top of the surface layer, assumed 10% of the boundary layer height, and $\nu_k = 0.4$ is the von Kármán constant. The PBL height is calculated, similarly to Nielsen-Gammon et al. (2008), as the level at which the potential temperature first exceeds the minimum potential temperature within the boundary layer by 1.5 K. The similarity functions are defined as

$$\phi_m = \begin{cases} 1 + 4.7\dfrac{z}{L} & \text{if } \dfrac{z}{L} \geq 0 \\ \left(1 - 16\dfrac{z}{L}\right)^{-1/4} & \text{if } \dfrac{z}{L} < 0 \end{cases}, \quad (9a)$$

$$\phi_h = \begin{cases} 1 + 4.7\dfrac{z}{L} & \text{if } \dfrac{z}{L} \geq 0 \\ \left(1 - 16\dfrac{z}{L}\right)^{-1/2} & \text{if } \dfrac{z}{L} < 0 \end{cases}, \quad (9b)$$

where L is the Obukhov length (Monin and Obukhov 1954).

b. The correction term for the ε equation

The standard K–ε model does not work well for flows with large mean shear, spreading of jets, or rotating turbulence (Shih et al. 1995). In fact, several terms in the exact dissipation rate equation are unknown. For this reason, the dissipation rate equation [Eq. (7)] was created with a similar structure as the TKE equation, by assuming that the source and sink terms of the dissipation rate are proportional to the source and sink terms of TKE times the large eddy turnover time scale K/ε. To improve the standard model for the stable atmosphere, Zeng et al. (2020) introduced an additional source term A_ε in the buoyancy term of the dissipation rate equation, to represent the dependence of energy drain on the eddy scale:

$$A_\varepsilon = c_4 \min\left(1, \sqrt{\frac{\text{Ri}}{c_5}}\right)N\varepsilon, \quad (10)$$

where Ri is the gradient Richardson number Ri = $(g/\Theta_0)\{(\partial\Theta/\partial z)/[(\partial U/\partial z)^2 + (\partial V/\partial z)^2]\}$; N is the Brunt–Väisälä frequency $N = [(g/\Theta_0)(\partial\Theta/\partial z)]^{1/2}$; g is the gravitational acceleration; and Θ_0 is the reference temperature, set to 290 K; while c_4 and c_5 are constants chosen to be consistent with the MOST, and set equal to 0.44 and 0.08, respectively. This additional term acts only in case of stable atmosphere (i.e., when the Richardson number is greater than zero, then in the convective boundary layer (CBL) it is nonzero only in the capping inversion layer).

c. The counter-gradient heat flux

Deardorff (1966) highlighted the need of considering a nonlocal term in the vertical heat flux parameterization, in order to take into account the effect of large eddies and surface-driven motions in unstable conditions. It allows a vertical transport of heat upward without a super-adiabatic lapse rate. The nonlocal counter-gradient term, acting only within the PBL, enters in the parameterization of the vertical heat flux, which can be written as

$$\overline{w\theta} = -\nu_H\left(\frac{\partial\Theta}{\partial z} - \gamma\right), \quad (11)$$

and γ is parameterized following Troen and Mahrt (1986):

$$\gamma = C \frac{\overline{w\theta_s}}{w_\star h}, \qquad (12)$$

where $C = 10$, $\overline{w\theta_s}$ is the surface heat flux, and $w_\star = [(g/\Theta_0)h\overline{w\theta_s}]^{1/3}$ is the convective velocity scale. The above mentioned counter-gradient is largely adopted in state-of-the-art PBL parameterizations, demonstrating its ability in reducing instabilities and in better describing the vertical temperature profile (Ching et al. 2014).

d. The temperature variance equation

The countergradient term does not act in stably stratified regimes, when turbulence production has actually been observed (Mauritsen et al. 2007) and parameterized (Zilitinkevich et al. 2007, 2013). So, its efficiency is limited only to unstable regimes; therefore for stable regimes an additional term should be considered. Standard models usually assume a critical Richardson number (~0.25) above which turbulence is completely damped. To consider even turbulence in stably stratified regimes, similarly to Lazeroms et al. (2016) and Želi et al. (2019), besides the prognostic equations for K [Eq. (4)] and ε [Eq. (7)], we added a prognostic equation for the half of the temperature variance [$K_\theta = (1/2)\overline{\theta^2}$], that reads as

$$\frac{\partial K_\theta}{\partial t} = -\frac{\partial \overline{wK_\theta}}{\partial z} - \overline{w\theta}\frac{\partial \Theta}{\partial z} - \varepsilon_\theta, \qquad (13)$$

where the terms on the right-hand side represent the turbulent transport, the production/destruction by buoyancy and the dissipation, respectively. The dissipation term is parameterized as

$$\varepsilon_\theta = \frac{K_\theta}{\tau R}, \qquad (14)$$

where $\tau = K/\varepsilon$ is the large eddy turnover time scale and

$$R = \frac{2}{3\left(1 + \dfrac{\overline{w\theta^2}}{KK_\theta}\right)} \qquad (15)$$

as described in Craft et al. (1996).

In Eq. (15) K_θ is proportional to the turbulent potential energy (TPE), which is defined as

$$TPE = \frac{1}{2}\frac{g}{\Theta_0}\frac{\overline{\theta^2}}{\dfrac{\partial \Theta}{\partial z}} \qquad (16)$$

The main idea of adopting a prognostic equation for K_θ (or TPE) is to take into account the conversion between TKE and TPE depending on the vertical stratification; K_θ acts both in stable and in unstable boundary layers, as a counter-gradient, analogous to the γ term introduced above. In particular, it enters the computation of the vertical heat flux, which now is calculated as (Lazeroms et al. 2016):

$$\overline{w\theta} = -\nu_H\frac{\partial \Theta}{\partial z} + \Phi_{cg}, \qquad (17)$$

where

$$\Phi_{cg} = c_\mu \frac{g}{\Theta_0}\frac{KK_\theta}{\varepsilon}. \qquad (18)$$

Its effect is larger in areas with large temperature fluctuations (i.e., large K_θ), thus in the surface layer and in the inversion layer, where temperature gradients are stronger than in the other regions. The term Φ_{cg} replaces the counter-gradient term of Eq. (12). Differently from γ, which is null, in stable regimes $\Phi_{cg} > 0$.

e. The numerical solver

Equations for wind speed, potential temperature, and water vapor mixing ratio are solved implicitly, using the tridiagonal matrix algorithm, adding source and sink terms at the surface (as explained later). For the coupled equations of K and ε, a more complex method is needed, since the strong nonlinearities may interact with discretization errors in such a way to destabilize computation (Lew et al. 2001).

Substituting the flux-gradient relation into the respective fluxes [Eq. (2)], and neglecting the first temporal step of the turbulent transport term [first term on the right hand side of Eqs. (4) and (7)] and the counter-gradient term [Eqs. (12) or (18)], which will be added later, since it is always stable using the tridiagonal matrix, we obtain

$$\frac{\partial K}{\partial t} = c_\mu\left(S^2 - \frac{N^2}{Pr}\right)\frac{K^2}{\varepsilon} - \varepsilon, \qquad (19a)$$

$$\frac{\partial \varepsilon}{\partial t} = c_\mu\left(c_1 S^2 - c_3\frac{N^2}{Pr}\right)K - c_2\frac{\varepsilon^2}{K}, \qquad (19b)$$

where $S^2 = (\partial U/\partial z)^2 + (\partial V/\partial z)^2$ is the wind shear and N^2 the squared Brunt–Väisälä frequency.

Introducing the new variables $X = K/\varepsilon$ and $Y = \varepsilon^\alpha K^\beta$, and differentiating opportunely, we obtain a set of two decoupled equations:

$$\frac{\partial X}{\partial t} = -CX^2 + (c_2 - 1), \qquad (20a)$$

$$\frac{\partial \ln Y}{\partial t} = (\alpha A + \beta B)X - (\alpha + \beta c_2)\frac{1}{X}, \qquad (20b)$$

with

$$A = c_\mu\left(S^2 - \frac{N^2}{Pr}\right), \qquad (21)$$

$$B = c_\mu\left(c_1 S^2 - c_3\frac{N^2}{Pr}\right), \qquad (22)$$

and

$$C = B - A = c_\mu \left[(c_1 - 1)S^2 - (c_3 - 1)\frac{N^2}{\mathrm{Pr}} \right]; \qquad (23)$$

C can be either positive or negative, depending on the sign and magnitude of buoyancy. This set of equations has an analytical solution. X has three possible solutions, depending on the sign of C. For $C = 0$ the solution is simple:

$$X^{n+1} = X^n + (c_2 - 1)\Delta t. \qquad (24)$$

For $C > 0$:

$$X^{n+1} = \frac{\tanh\left[a \tanh\left(\frac{\sqrt{C} X^n}{\sqrt{c_2 - 1}} \right) + \sqrt{C}\,\Delta t\,\sqrt{c_2 - 1} \right]\sqrt{c_2 - 1}}{\sqrt{C}}. \qquad (25)$$

For $C < 0$:

$$X^{n+1} = -\frac{\sqrt{1 - c_2}\,[\tan(\sqrt{-C}\,\Delta t\,\sqrt{1 - c_2})\,\sqrt{1 - c_2} - \sqrt{-C}\,\Delta t]}{\sqrt{-C}\,[\sqrt{1 - c_2} + \sqrt{-C}\,X^n\,\tan(\sqrt{-C}\,\Delta t\,\sqrt{1 - c_2})]}. \qquad (26)$$

For Y the solution is obtained, assuming $\alpha = 1$ and $\beta = -1/c_2$, by eliminating the second term in Eq. (20b), to simplify the numerical computation:

$$Y^{n+1} = Y^n \exp\left[\Delta t\, X^{n+1}\left(A - \frac{B}{c_2} \right) \right]. \qquad (27)$$

After solving these coupled equations, K and ε are calculated inverting X and Y, and then the turbulent transport term is added to both variables. The analytical solution has the advantage of being stable for every time step Δt and it is not affected by numerical approximations errors.

The equation for K_θ [Eq. (13)] is solved separately from the K–ε system of equations. Expanding all the terms, the equation for the temperature variance reads

$$\frac{\partial K_\theta}{\partial t} = +\frac{\partial}{\partial z}\left(\nu_M \frac{\partial K_\theta}{\partial z} \right) + \nu_H \left(\frac{\partial \Theta}{\partial z} \right)^2 - c_\mu \frac{g}{\Theta_0} \frac{K K_\theta}{\varepsilon} \frac{\partial \Theta}{\partial z} - \frac{K_\theta \varepsilon}{R K}. \qquad (28)$$

This equation can be solved by applying the Thomas's tridiagonal algorithm (Lee 2011) for the diffusion part, and treating explicitly the second term on the right-hand side, while the other two are treated implicitly since they depend on K_θ.

The equation for potential temperature then becomes

$$\frac{\partial \Theta}{\partial t} = \frac{\partial}{\partial z}\left(\nu_M \frac{\partial \Theta}{\partial z} \right) - \frac{\partial \Phi_{\mathrm{cg}}}{\partial z}. \qquad (29)$$

f. Initial and boundary and conditions

Regarding the initial conditions for the simulations, we set the values $K_0 = 10^{-4}$ m^2 s^{-2}, $\varepsilon_0 = 10^{-7}$ m^2 s^{-3}, and $K_{\theta 0} = 10^{-7}$ K for all the columns of air. As boundary conditions, we set K, ε, and K_θ at their minimum value at the top of the simulation domain.

On the other hand, at the surface, we use a mix of Neumann and Dirichlet boundary conditions. For U, V, and Θ we assume Neumann boundary conditions as already done in WRF for the Bougeault and Lacarrere (1989) closure:

$$\frac{\partial U_1}{\partial t} = -\frac{u_\star^2}{\Delta z_1 |U_{\mathrm{TOT}}|}\, U_1, \qquad (30a)$$

$$\frac{\partial V_1}{\partial t} = -\frac{u_\star^2}{\Delta z_1 |U_{\mathrm{TOT}}|}\, V_1, \qquad (30b)$$

$$\frac{\partial \Theta_1}{\partial t} = \frac{\overline{w\theta_s}}{\Delta z_1}, \qquad (30c)$$

where the subscript "1" refers to the variable calculated at the center of the first grid cell close to the surface, $u_\star$ is the friction velocity, and Δz_1 is the height of the first level. For K and ε, we assume Dirichlet boundary conditions, adopting MOST (Hartogensis and De Bruin 2005; van der Laan et al. 2017):

$$K_1 = \frac{u_\star^2}{\sqrt{c_\mu}}\sqrt{\frac{\phi_\varepsilon}{\phi_m}}, \qquad (31a)$$

$$\varepsilon_1 = \frac{u_\star^3}{v_k \frac{\Delta z_1}{2}}\,\phi_\varepsilon, \qquad (31b)$$

where

$$\phi_\varepsilon = \begin{cases} \left[1 + 2.5\left(\frac{z}{L} \right)^{0.6} \right]^{3/2} & \text{if } \frac{z}{L} \geq 0 \\ 1 - \frac{z}{L} & \text{if } \frac{z}{L} < 0 \end{cases}. \qquad (32)$$

For K_θ, we assume again Neumann boundary conditions, employing in Eq. (13) the boundary conditions in Eqs. (30c), (31a), and (31b).

3. Setup and case studies

In this study the Advanced Research version of the Weather Research and Forecasting (WRF) Model, version 4.1, is used for the numerical simulations (Skamarock et al. 2019). WRF has been successfully applied in several studies for idealized cases for both RANS simulations and LES, both in flat (Zhang et al. 2018; Moeng et al. 2007) and in complex terrain (Schmidli et al. 2011; Wagner et al. 2014). The third-order Runge–Kutta method is used for time integration for all the simulations in this study. In LES mode, we use the 1.5-order 3DTKE model for the subgrid turbulence parameterization (Deardorff 1980). We take a three-dimensional average of 20 different LES, differing in the initial random potential temperature perturbation, with amplitude of 0.1 K and zero mean, applied at the first four vertical layers, necessary to trigger turbulence at the initial time step. For the very stable case study (viz. GABLS) LES are the ones used in Beare et al. (2006) (available at https://gabls.metoffice.com/lem_data.html). LES are considered as our reference for each case

TABLE 1. Schematic overview of the different case studies.

	PBL type	dT_S/dt (K h^{-1})	$d\Theta_0/dz$ (K km^{-1})	Terrain	U_g (m s^{-1})	V_g (m s^{-1})	Domain size (km × km × km)
CBL_F_3	Convective	3.5	3.3	Flat	0	10	10 × 10 × 3
CBL_F_10	Convective	3.5	10	Flat	0	10	10 × 10 × 3
CBL_V_NOW	Convective	3.5	3.3	Valley	0	0	40 × 10 × 5
CBL_V_W	Convective	3.5	3.3	Valley	0	10	40 × 10 × 5
GABLS	Stable	−0.25	10	Flat	8	0	10 × 10 × 1

analyzed, and are compared with RANS simulations performed with the novel K–ε schemes presented here, which have been implemented in the WRF Model, and with other conventional 1D PBL schemes already implemented in the standard version of the WRF Model. These PBL schemes are the BouLac (Bougeault and Lacarrere 1989), the Mellor–Yamada–Nakanishi–Niino level 2.5 without the mass-flux component (MYNN2.5; Nakanishi and Niino 2004) and the Yonsei State University (YSU; Hong et al. 2006) schemes. Moreover, the comparison is performed with a K–ε-based scheme (E–ε hereafter, Zhang et al. 2020), introduced in WRF 4.3, and implemented for this work in WRF 4.1. Both RANS simulations and LES are performed with a time step of 0.5 s, for a 4-h period (with the exception of the GABLS simulations, which cover 9 h). Lateral boundary conditions in both W–E and S–N directions are periodic, allowing to replicate an infinite domain. The results from the different RANS simulations are compared with the LES considering the hourly average values computed on all the time steps between the third and the fourth hour of simulation, when the PBL is well developed. Similarly, simulation outputs are averaged horizontally, in order to compare model results on a single column value for the flat cases (average in both horizontal directions) and on a cross-valley section for the valley cases (average along the south-north direction). All simulations are performed for a dry atmosphere, with zero humidity both in the air and in the soil. In this study, five different cases (summarized in Table 1) are considered, varying in thermal stratification, surface temperature forcing, orography, and geostrophic wind. In section 4 we will present the comparison, for the five case studies, between each reference LES, the aforementioned conventional PBL schemes, and two different versions of the K–ε closure: the first experiment (K–ε–γ hereafter) assuming a counter-gradient term dependent only on the surface-layer features, calculated as in Eq. (12), and the second experiment (K–ε–θ^2 hereafter), in which the equation for the temperature variance is calculated from Eq. (13) and the counter-gradient term is computed using Eq. (18). Moreover, in the stable case (called GABLS hereafter), we run the K–ε–θ^2 closure also removing the additional term in the buoyancy production of the dissipation rate equation [Eq. (10)], in order to evaluate its contribution in improving the reproduction of the PBL in stable regimes (K–ε–θ^2–NOA$_\varepsilon$ hereafter).

a. CBL on flat terrain

We assume a homogeneous terrain and a PBL in convective conditions, similar to Zhang et al. (2018). The simulation is performed over a 10 km × 10 km domain with a horizontal grid size of 50 m and 1 km for LES and RANS simulations, respectively. The model top is at 3 km, with 150 equally spaced vertical layers (i.e., the depth of each layer is 20 m). The CBL is driven by a constant surface heating rate of 3.5 K h^{-1}, with an initial surface skin temperature of 300 K, and geostrophic wind in the N–S direction of 10 m s^{-1}, constant along the vertical, with Coriolis forcing turned off. We tested two cases, differing in the intensity of the unperturbed thermal stratification. The initial potential temperature sounding is

$$\theta = \begin{cases} 300 & \text{if } z \leq 100 \text{ m} \\ 300 + (z - 100 \text{ m})\Gamma & \text{if } z > 100 \text{ m} \end{cases}, \quad (33)$$

with Γ = 3.3 K km^{-1} for the case with a weakly stable initial stratification (CBL_F_3 hereafter), and Γ = 10 K km^{-1} for the case with a very stable initial stratification (CBL_F_10 hereafter).

b. CBL in an idealized valley

Here we consider a W–E symmetric valley, infinite in the S–N direction, with sidewall crests at 1500 m. The analytical expression for the topography, identical to the one used in Schmidli et al. (2011), is given by

$$h(x) = 1500 \times \begin{cases} \frac{1}{2} - \frac{1}{2}\cos\left(\pi \frac{|x| - X_1}{S_x}\right) & X_1 < |x| < X_2 \\ 1 & X_2 < |x| < X_3 \\ \frac{1}{2} + \frac{1}{2}\cos\left(\pi \frac{|x| - X_3}{S_x}\right) & X_3 < |x| < X_4 \end{cases} \quad (34)$$

with sloping sidewall width S_x = 9 km, and X_1 = 0.5 km, X_2 = 9.5 km, X_3 = 10.5 km, and X_4 = 19.5 km. Simulations are performed over a 40 km × 10 km domain, to ensure a coherent reproduction of the cross-valley circulation in the RANS simulations. The horizontal grid size is 50 m and 1 km for LES and RANS simulations, respectively, as in the flat case. The model top is at 5 km with 250 hybrid sigma–pressure vertical layers. Hybrid levels are chosen in order to reduce upper-level disturbances which, in terrain-following coordinates, can be produced by the advection of strong horizontal flow perturbed by the terrain influence (Park et al. 2019). The CBL is driven by a surface heating rate of 3.5 K h^{-1} and the initial surface skin temperature is the same of the first atmospheric layer. The initial vertical temperature profile is the same as in the CBL_F_3 case. We test two different cases for the valley configuration: one with null initial wind (CBL_V_NOW hereafter),
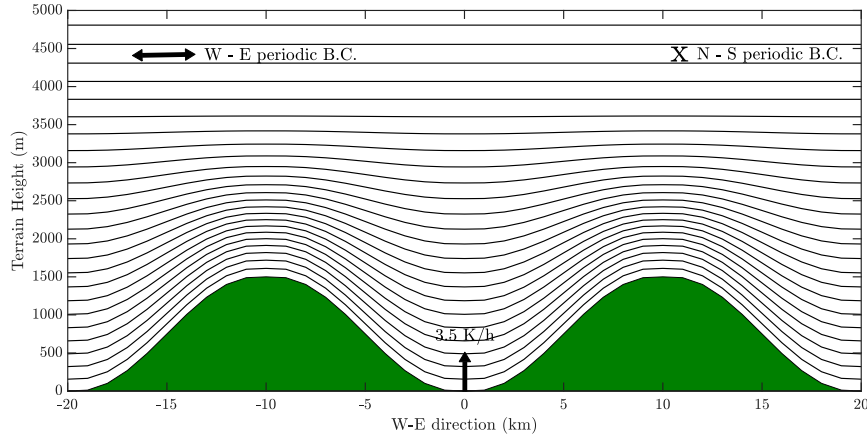
FIG. 1. Design of the domain, forcing, and boundary conditions for the valley cases. Vertical layers are plotted with an interval of 10.

and one with a constant wind of 10 m s^{-1} in the S–N direction (CBL_V_W hereafter). This wind is imposed in the initial conditions with the aim of reproducing an along valley wind, usually present with the development of thermally driven circulations, and deeply studied through observations (Giovannini et al. 2017) and numerical simulations (Rampanelli et al. 2004). The design of the idealized simulations in the valley case is reported in Fig. 1. In this case, LES results are averaged along the W–E section of the valley, using the RANS simulations grid as query grid, in order to allow a meaningful comparison with the results from the RANS simulations.

c. SBL in flat terrain

This case is based on the simulations of an Arctic SBL [GEWEX Atmospheric Boundary Layer Study (GABLS)] presented in Kosović and Curry (2000), and subsequently used for the intercomparison of LES (Beare et al. 2006) and RANS (Cuxart et al. 2006) simulations, aiming to quantify the reliability of different PBL schemes through the comparison with observational data. The initial potential temperature profile consists of a mixed layer up to 100 m with a potential temperature of 265 K, with an overlying inversion with $\Gamma = 10$ K km^{-1}. A surface cooling rate of 0.25 K h^{-1} is applied for 9 h, so a quasi-equilibrium state is reached. The geostrophic wind is set to 8 m s^{-1} in the W–E direction, with a Coriolis parameter of 1.39×10^{-4} s^{-1}.

For this case study, we take as reference the LES presented in Beare et al. (2006) at 3.125-m vertical and horizontal resolution [viz., CORA, CSU, IMUK, LLNL, NCAR, NERSC, and UIB in Beare et al. (2006)]. They are produced by different NWP models and adopt various subgrid turbulence closures. The simulation domain is a box of 400 m × 400 m × 400 m, and simulations outputs are averaged spatially over the horizontal domain and temporally between the eighth and ninth hour of the simulation. RANS simulations instead are run on a 10 km × 10 km horizontal domain; the top of the domain is set at 1 km above ground level, adopting a depth of 5 m for each vertical level.

d. Calculation of turbulent fluxes

Calculation of turbulent fluxes is performed differently for LES and RANS simulations. Turbulent fluxes for RANS simulations are computed in the same way for all turbulence parameterization schemes, through the tendency of each variable. If C is a variable of the mean flow ($C = U, V, \Theta$) from Eq. (1) it follows that, for each vertical layer:

$$\overline{wc}\big|_{n+1} - \overline{wc}\big|_n = -\int_n^{n+1} \frac{\partial C}{\partial t}\, dz, \tag{35}$$

where we impose a null flux at the top of the domain, and surface fluxes as in Eq. (30) for $n = 1$. On the other hand, vertical turbulent fluxes in LES consist in the sum of the resolved (RES) part and of the subgrid-scale (SGS) part:

$$\overline{wc} = \overline{wc}_{\text{RES}} + \overline{wc}_{\text{SGS}}. \tag{36}$$

The RES part is calculated directly from the model output, for each time step, and then averaged temporally over 1 h. The mean variables (capital letters) are calculated as a temporal average over 1 h:

$$\overline{wc}_{\text{RES}} = \overline{(w - W)(c - C)}, \tag{37}$$

while the SGS is calculated as

$$\overline{wc}_{\text{SGS}} = -K_{\text{CV}}\frac{\partial C}{\partial z}, \tag{38}$$

where K_{CV} is the vertical diffusivity coefficient for the mean variable C, calculated as in Deardorff (1966). RANS turbulent fluxes are then averaged temporally over an hour, and spatially over the entire domain for the flat cases, and over a W–E section for the valley cases.

4. Results

This section presents the results of the comparison between the idealized RANS simulations with the different PBL schemes and the LES, for the different case studies shown in Table 1. In
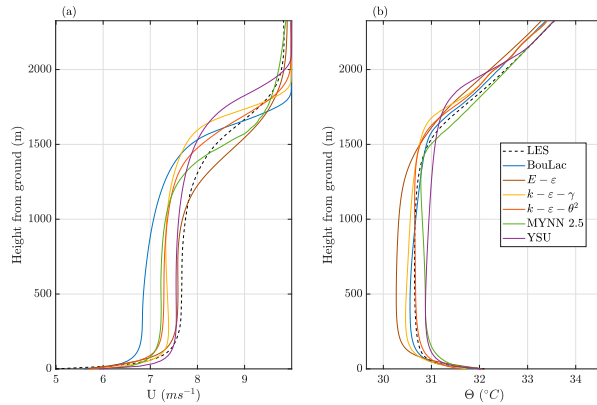
FIG. 2. Vertical profiles of (a) wind speed and (b) potential temperature for the CBL_F_3 case. The dashed black line refers to the ensemble of LES, while colored lines refer to the different RANS simulations.
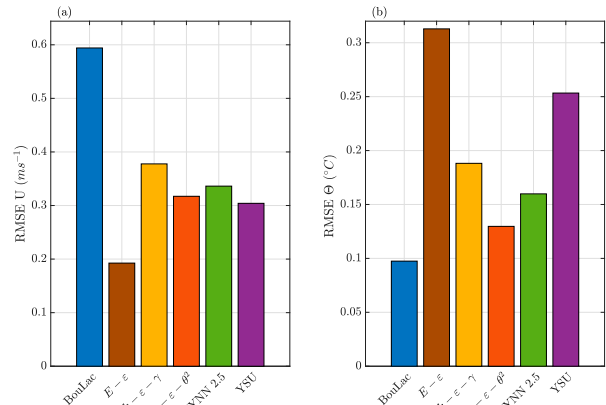

FIG. 3. Root-mean-square error (RMSE) for each RANS simulation with respect to the reference LES, calculated for an air column up to 2050 m above ground level for the CBL_F_3 case, for (a) wind speed and (b) potential temperature.

the following subsections (4a, 4b, and 4c), the presentation of the results for the different case studies is separated between CBL in flat terrain (CBL_F_3,CBL_F_10), CBL in an idealized valley (CBL_V_NOW,CBL_V_W), and SBL in flat terrain (GABLS), respectively.

a. CBL in flat terrain

Figure 2 shows the vertical profiles of wind speed (left) and potential temperature (right) for the CBL_F_3 case, considering the temporal average between the third and the fourth hour of time integration. The profile is typical of a CBL, with a surface layer ~150 m deep and a PBL height of ~1500 m. The wind speed follows this pattern, approaching ~10 m s^{-1} over the PBL, remaining almost constant in the mixed layer and rapidly decreasing to ~5 m s^{-1} in the first vertical level. All RANS simulations reasonably agree with the LES in terms of potential temperature. In particular, K–ε–θ^2 outperforms the other schemes within the surface layer, while BouLac is the best in reproducing the capping inversion over the mixed layer. On the other hand, YSU overestimates the PBL height, while MYNN2.5 exhibits a quasi-unstable boundary layer instead of a mixed layer. E–ε well performs in terms of gradients, but it underestimates the temperature in the mixed layer, because of a too deep surface layer, and underestimates the height of the PBL. K–ε–γ reasonably reproduces the mixed layer, but it overestimates the absolute value of the potential temperature gradient in the surface layer, and it slightly overestimates the PBL height. Regarding the wind speed profile, YSU and E–ε are the best in reproducing the vertical profile within the surface and the mixed layer, but, as for the potential temperature, the overestimation (underestimation) of the PBL height leads to an underestimation (overestimation) of wind speed in the capping layer, respectively. Despite a good performance in terms of potential temperature, BouLac fails in reproducing the wind profile in the mixed layer, while MYNN2.5 underestimates the wind speed in the capping layer. K–ε–θ^2, instead, performs similarly to MYNN2.5 in the mixed layer, but it is the best simulation

in reproducing the wind shear in the capping layer. K–ε–γ performs similarly to K–ε–θ^2, but again overestimating the PBL height and then underestimating the wind speed in the capping layer.

To quantify the ability of the RANS simulations in reproducing wind speed and potential temperature in the CBL, in Fig. 3 we show the root-mean-square error (RMSE), calculated along the air column, between each RANS simulation and the reference LES. K–ε–γ, K–ε–θ^2, MYNN2.5, and YSU show RMSE ~ 0.3–0.35 m s^{-1} for the wind speed, while in BouLac the RMSE is considerably higher (~0.6 m s^{-1}). The best results are shown by E–ε, with an error of ~0.2 m s^{-1}. On the other side, BouLac is the best in reproducing the potential temperature profile (RMSE ~ 0.1°C), followed by K–ε–θ^2 and MYNN2.5. The highest errors are shown by K–ε–γ, YSU and E–ε, since the first two overestimate the height of the inversion layer, while the latter cannot reproduce correctly the temperature in the mixed layer.
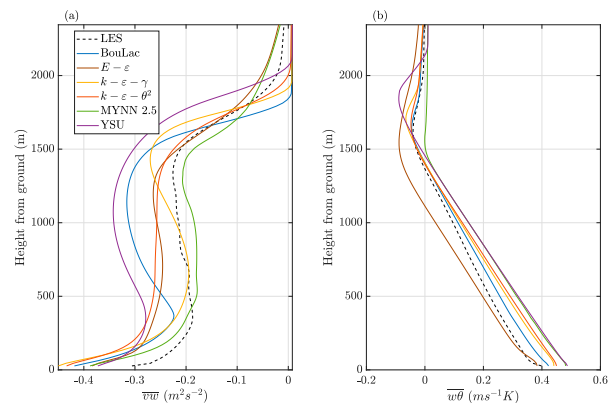

FIG. 4. Vertical profiles of (a) vertical momentum flux and (b) vertical heat flux for the CBL_F_3 case. The dashed black line refers to the ensemble of LES, while colored lines refer to the different RANS simulations.
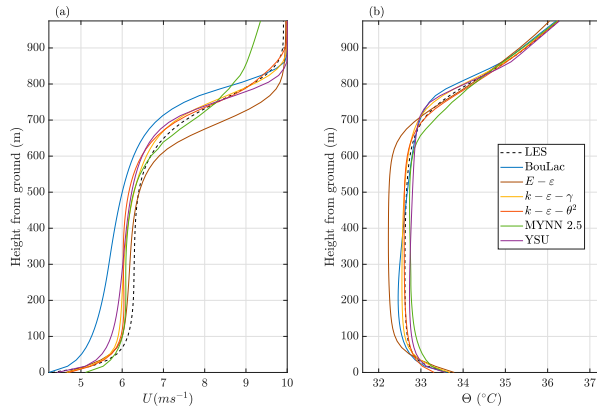
FIG. 5. Vertical profiles of (a) wind speed and (b) potential temperature for the CBL_F_10 case. The dashed black line refers to the ensemble of LES simulations, while colored lines refer to the different RANS simulations.

FIG. 7. Vertical profiles of (a) vertical momentum flux and (b) vertical heat flux for the CBL_F_10 case. The dashed black line refers to the ensemble of LES simulations, while colored lines refer to the different RANS simulations.

Figure 4 reports the vertical profiles of the vertical heat flux (left) and of the vertical momentum flux (right). $\overline{w\theta}$ is well reproduced by all the simulations apart for E–ε, up to the inversion layer. Here, BouLac and K–ε–θ^2 better reproduce the negative peak in the inversion layer with respect to the others. On the other side, all RANS simulations overestimate the intensity of $\overline{uw}$ in the surface layer, while, the two K–ε and E–ε are the best in reproducing the decrease of the vertical momentum flux above the top of the PBL, with a better agreement in terms of gradient and thickness of this layer. Moreover, BouLac and YSU overestimate the intensity of $\overline{uw}$ in the upper part of the mixed layer.

Figure 5 shows the vertical profiles of wind speed (left) and potential temperature (right) for the CBL_F_10 case. This case differs from the previous one only in the initial vertical temperature gradient, which is now set to 10 K km^{-1}. Due to this stronger stratification, the PBL height reaches a depth of ~800 m, with a less unstable surface layer with respect to the previous case. While there are no relevant differences between the RANS
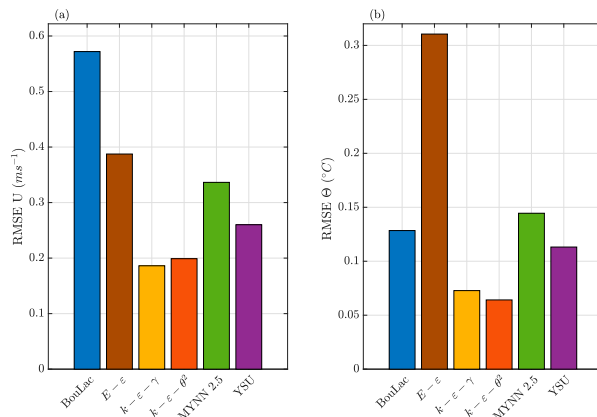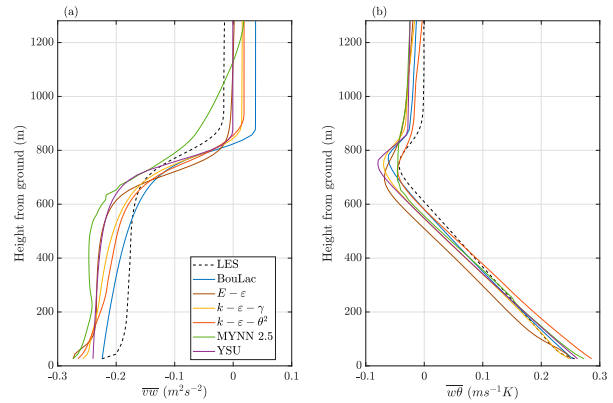

FIG. 6. Root-mean-square error (RMSE) for each RANS simulation with respect to the reference LES, calculated for an air column up to 1000 m for the CBL_F_10 case, for (a) wind speed and (b) potential temperature.

simulations in the surface layer, in the mixed layer and in the entrainment zone K–ε–θ^2 provides the best results regarding the temperature profile, followed by K–ε–γ. On the other hand, YSU and BouLac overestimate, while MYNN2.5 and E–ε underestimate the inversion layer height. In particular, E–ε cannot reproduce the slope of the temperature profile, probably due to a too low value of the counter-gradient term. Improvements by the K–ε schemes are found even in reproducing the wind speed, with best results again in the capping layer. Again, BouLac shows a too low wind speed in the mixed layer, while MYNN2.5 over the capping layer. RMSEs (Fig. 6) show indeed the lowest values for the two K–ε schemes, even one-third with respect to the other RANS simulations for the potential temperature. They are followed by YSU, while MYNN2.5 and BouLac and E–ε are the worst, since they cannot capture precisely the capping layer height. Even for the turbulent fluxes (Fig. 7), better results are found for K–ε–θ^2: while in the surface and mixed layers it is not possible to identify particular differences between the different RANS simulations, at the inversion layer the new turbulence scheme can better reproduce the negative peak of the vertical heat flux (left) and the slope of the vertical momentum flux (right).

b. CBL in an idealized valley

In this subsection, the results from the simulations for the idealized valley are presented. Figure 8 shows the cross-valley section of zonal wind (left), potential temperature (middle), and meridional wind (right) averaged along the N–S direction and from the third to the fourth hour of simulation for the CBL_V_W case study for the reference ensemble of LES (CBL_V_NOW shows similar patterns for U and Θ). A cross-valley circulation is well distinguishable from the zonal wind speed panel, with two cross-valley circulation cells on top of each other, similar to those identified in Wagner et al. (2014). Upslope winds are weaker close to the valley floor, and they reach a maximum value of ~4 m s^{-1} close to the ridge. A return flow toward the center of the valley is evident between 1500 and 2500 m: warmer air is advected from the ridge top to
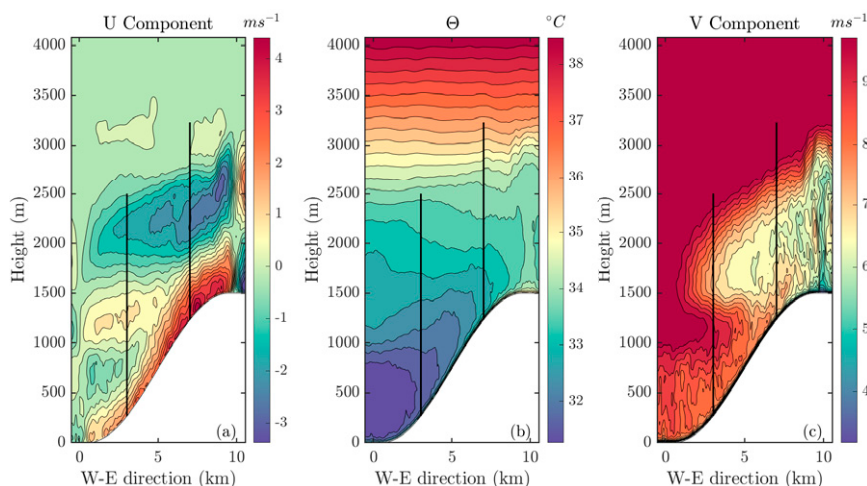
FIG. 8. Zonal section of (left) zonal wind speed, (center) potential temperature, and (right) meridional wind speed, for the ensemble of LES of the CBL_V_W case study. Vertical black lines refer to the position of vertical profiles shown in Figs. 9 and 12 for the lower point, and in Figs. 10 and 13 for the upper point along the slope.

the center of the valley, despite the presence of an underlying smaller thermal convective cell, in analogy with what found in Serafin and Zardi (2010). Because of this return flow, the potential temperature profile exhibits a double mixed layer, one over the surface layer, and the second at the level of the return-flow layer. The presence of upslope circulations along the ridges increases the wind shear, decreasing the meridional wind speed through increased turbulence production. Indeed, the vertical profile of meridional wind speed (right panel of Fig. 8) is not constant along the valley slope, but it is influenced by the branch of the upslope circulation pointing toward the center of the valley. As a consequence, above the ridge level, the meridional wind speed is lower.

Figure 9 shows the vertical profiles of zonal wind speed (left) and potential temperature (right) for a point along the

eastern slope situated at 267 m above the valley floor for the CBL_V_NOW case study. The zonal wind speed presents four different peaks, with the lowest and the highest ones more intense than the other two in absolute value, representing the two convective cells described before (negative values represent air moving from the ridge to the valley center). All RANS simulations are able to capture the double circulation along the vertical, but with some errors. In particular, YSU overestimates the height of the three upper peaks, BouLac and MYNN2.5 overestimates the third peak, E–ε underestimates the first peak and overestimates the third, while the two K–ε underestimate the second and the fourth peak, but they are the best in reproducing the third peak.

Regarding the potential temperature profile, the two K–ε schemes better describe the surface layer and the lower mixed
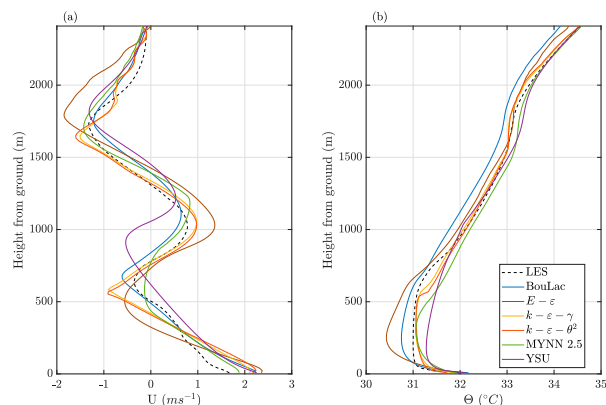

FIG. 9. Vertical profiles of (a) zonal wind speed and (b) potential temperature for the CBL_V_NOW case for a point situated at 267 m above the valley floor on the eastern slope. The dashed black line refers to the ensemble of LES, while colored lines refer to the different RANS simulations.
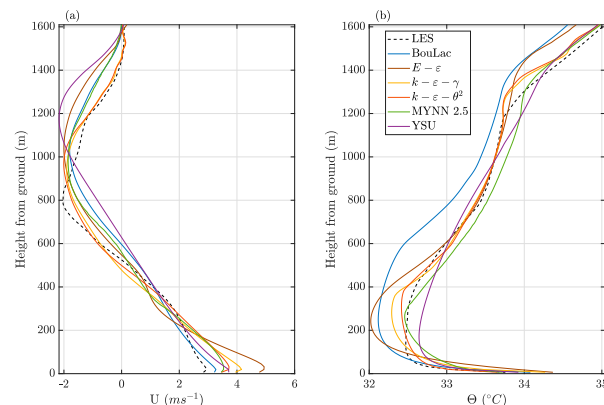
FIG. 10. Vertical profiles of (a) zonal wind speed and (b) potential temperature for the CBL_V_NOW case for a point situated at 1232 m above the valley floor on the eastern slope. The dashed black line refers to the ensemble of LES, while colored lines refer to the different RANS simulations.
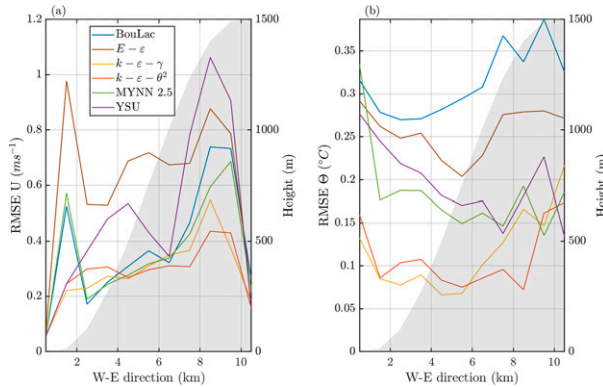
FIG. 11. RMSEs of (a) zonal wind speed and (b) potential temperature with respect to the ensemble of LES, calculated as the average of the first 170 vertical levels for each point from the valley floor to the eastern ridge, for the CBL_V_NOW case for each RANS simulation. The background gray area represents the height above the valley floor along the W–E direction.

layer and inversion, while the others cannot capture correctly the height of the lower inversion (BouLac, E–ε, and MYNN2.5) or underestimate its gradient (YSU). All RANS simulations can capture the higher mixed layer above the ridge level, with a better performance of the two K–ε, both in terms of depth and absolute value.

Figure 10 shows the vertical profiles of zonal wind speed (left) and potential temperature (right) for a point along the eastern slope situated at 1232 m above the valley floor, i.e., where only the upper cell is present, for the CBL_V_NOW case study. For this reason, zonal wind vertical profiles display just the peak close to the surface and the peak of the return wind above the ridge

level (around 800 m above ground level). All RANS simulations capture the cell circulation, but E–ε overestimates the intensity of the first peak, and all PBL schemes overestimate the height of the second peak (in particular YSU). However, the two K–ε schemes get closer to the LES in representing the peak, and can better capture the decrease of wind speed with height (especially from 1200 to 1600 m above ground level). The two K–ε display better results considering especially the vertical profile of potential temperature (right panel of Fig. 10). In particular, K–ε–θ^2 shows a better agreement for the air column with respect to the other RANS simulations. BouLac underestimates the potential temperature along all the vertical profile, while E–ε fails to capture adequately the structure of the first mixed layer. Finally, MYNN2.5 often displays an overestimation, while YSU reproduce the presence of both the mixed layers.

To quantify the ability of each RANS simulation to reproduce the thermal circulation of the CBL_V_NOW case study, in Fig. 11 we show the RMSE, calculated along the first 170 vertical levels (~1800 m AGL), of zonal wind speed (left) and potential temperature (right) along the eastern slope of the valley. In general, the highest errors for the zonal wind are located in the parts of the slope close to the valley floor and close to the ridge, while they are very low where the wind tends to zero, i.e., above the valley floor and above the ridge. K–ε–θ^2 presents the lowest RMSE, always between 0.2 and 0.4 m s^{-1} in the central part of the slope. YSU is the worst in reproducing the wind profile in the highest part of the slope (RMSE up to 1 m s^{-1}), while E–ε presents the highest RMSE above the valley floor (up to 1 m s^{-1}).

Regarding the RMSE for potential temperature, again K–ε simulations show the best agreement with respect to the LES, especially in the lower part of the valley, followed
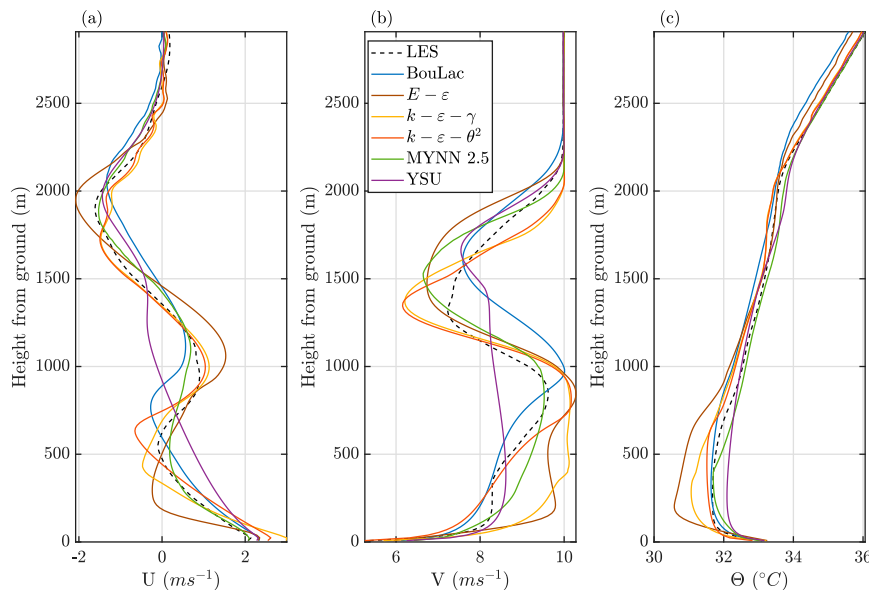

FIG. 12. Vertical profiles of (a) zonal wind speed, (b) meridional wind speed, and (c) potential temperature for the CBL_V_W case for a point situated at 267 m above the valley floor on the eastern slope. The dashed black line refers to the ensemble of LES, while colored lines refer to the different RANS simulations.
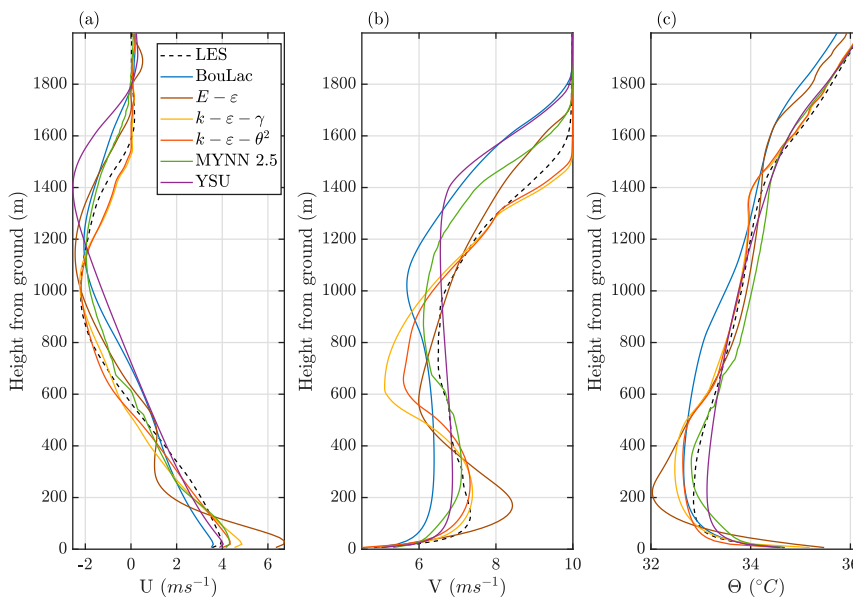
FIG. 13. Vertical profiles of (a) zonal wind speed, (b) meridional wind speed, and (c) potential temperature for the CBL_V_W case for a point situated at 1232 m above the valley floor on the eastern slope. The dashed black line refers to the ensemble of LES, while colored lines refer to the different RANS simulations.

by MYNN2.5 and YSU. BouLac is constantly the worst in terms of potential temperature, due to its constant underestimation over all the vertical column, followed by $E–\varepsilon$. While $K–\varepsilon$ simulations maintain a constant value of the RMSE along the slope, YSU and MYNN2.5 errors increase approaching the valley floor. For all RANS simulations, the highest RMSEs are found above the valley floor and the ridge.

Figures 12 and 13 show the vertical profile of zonal wind speed (left), potential temperature (center), and meridional wind speed (right) for the CBL_V_W case, for two points situated on the eastern slope at 267 and 1232 m above the valley floor, respectively. CBL_V_W differs from CBL_V_NOW for an imposed meridional geostrophic wind of 10 m s^{-1}, with the aim of simulating an along-valley wind and its interaction with the cross-valley thermal circulation.
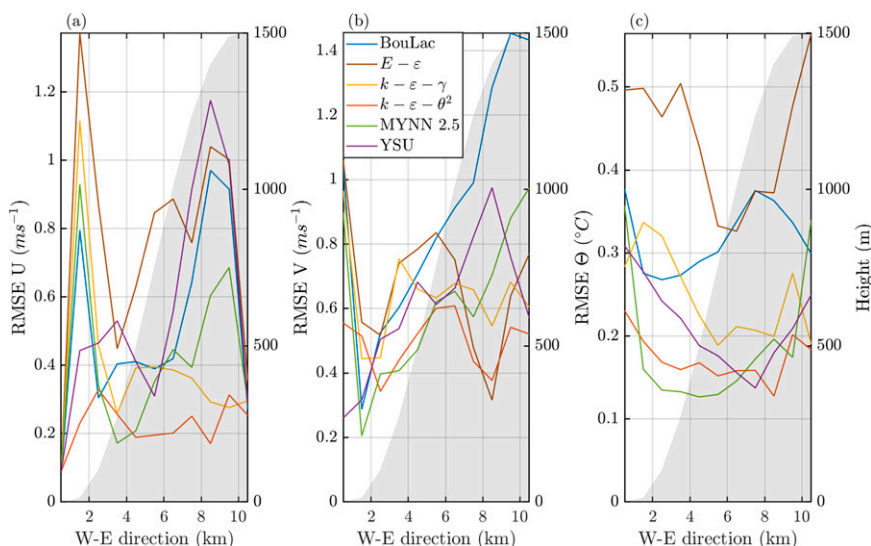

FIG. 14. RMSEs of (a) zonal wind speed, (b) meridional wind speed, and (c) potential temperature with respect to the ensemble of LES, calculated for the first 170 vertical levels for each point from the valley floor to the eastern ridge, for the CBL_V_W for each RANS simulation. The background gray area represents the height above the valley floor along the W–E direction.
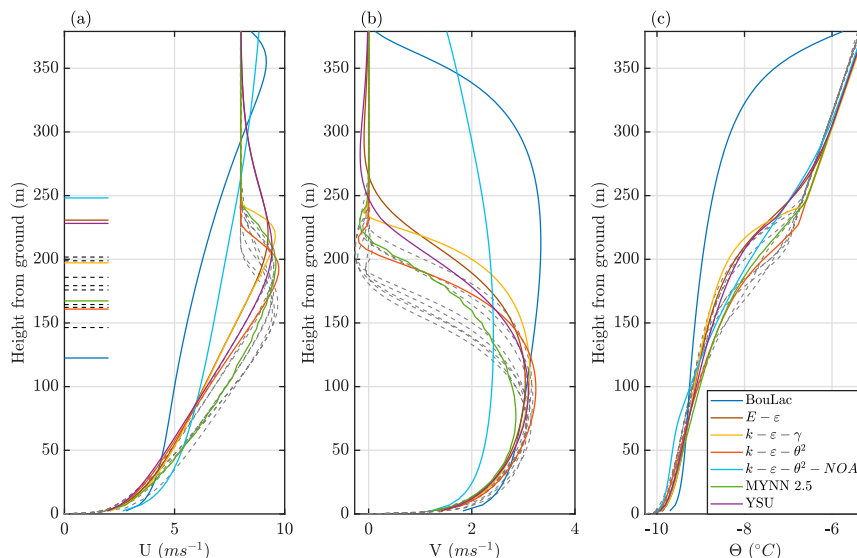
FIG. 15. Vertical profiles of (a) zonal wind speed, (b) meridional wind speed, and (c) potential temperature for the GABLS case. The horizontal lines on the left of (a) show the diagnostic boundary layer height for the RANS simulations and LES. The series of dashed gray lines refers to the different LES, while color lines refer to the RANS simulations.

Regarding the cross-valley wind and the potential temperature profiles, no substantial differences can be noticed with respect to the CBL_V_NOW case. K–ε–θ^2 is the most accurate in the simulation of both wind speed and potential temperature, especially in terms of potential temperature for the lower point (267 m above the valley floor) and of wind speed for the upper point (1232 m above the valley floor). The presence of the meridional wind causes stronger differences between the results of the two K–ε with respect to the CBL_V_NOW case. In fact, K–ε–θ^2 is more precise than K–ε–γ, since it better reproduces the up-slope wind intensity and the potential temperature in the surface layer at both heights. Most likely, the prognostic calculation of the counter-gradient flux in K–ε–θ^2 becomes more efficient, with respect to a diagnostic value (assumed by K–ε–γ), with the increasing complexity of PBL dynamics. Indeed, the largest improvements take place for the potential temperature in the lowest levels where, in unstable conditions, the temperature variance is larger with respect to the upper levels, as shown initially by Willis and Deardorff (1974). The vertical profile of the meridional wind is more complex than in the flat case (left panel in Fig. 2), especially for the point at 267 m above the valley floor. This is the effect of the cross-valley circulation: the thermal cross-valley circulation increases the wind shear and consequently increases the turbulence production, resulting in a decrease of wind speed in correspondence to the maximum wind shear. All RANS simulations, except for YSU, can capture the effect of the cross-valley thermal circulation on the along-valley meridional wind, and also the different intensity between the lower and upper points. The inefficiency of YSU in representing the vertical profiles of the along-valley wind is probably linked to the lack of a prognostic equation for TKE of this turbulence parameterization (developed for flat uniform terrains), since more complex

parameterizations become more efficient with increasing complexity (Chrobok et al. 1992). K–ε–θ^2 is the most efficient in capturing the height of the local minima and maxima of the along valley wind for the lower point, despite the overestimation (underestimation) of the maximum (minimum) at 900 m (1300 m). The same occurs for the higher point, even if the meridional wind speed is underestimated between 500 and 1000 m above the valley floor level. On the other hand, K–ε–θ^2 performs better with respect to the other RANS simulations (which overestimate the height of the inversion layer) in reproducing the meridional wind speed from 1000 to 1600 m, i.e., at the height of the inversion layer, for the upper point. Even for CBL_V_W, K–ε–θ^2 performs better with respect to K–ε–γ, especially in terms of the intensity of the various peaks.

Figure 14 displays the RMSE, calculated along the first 170 vertical levels, of the zonal wind speed (left), potential temperature (center), and meridional wind speed (right) for each point on the eastern slope of the valley. As in the CBL_V_NOW case, the two K–ε simulations perform better in the reproduction of the cross valley wind, especially for the points close to the ridge and to the valley floor. In this case, the difference between K–ε–θ^2 and K–ε–γ is higher, with the first that maintains good results close to the valley floor, where the performance of the other RANS simulations decreases significantly.

K–ε–θ^2 displays good results also for the potential temperature profile (middle panel). As for the CBL_V_NOW case, BouLac and E–ε present the worst results, since they always underestimate the potential temperature in the air column. In this case, MYNN2.5 performs similarly to K–ε–θ^2, while K–ε–γ fails to satisfactorily reproduce the potential temperature in the points close to the valley floor.
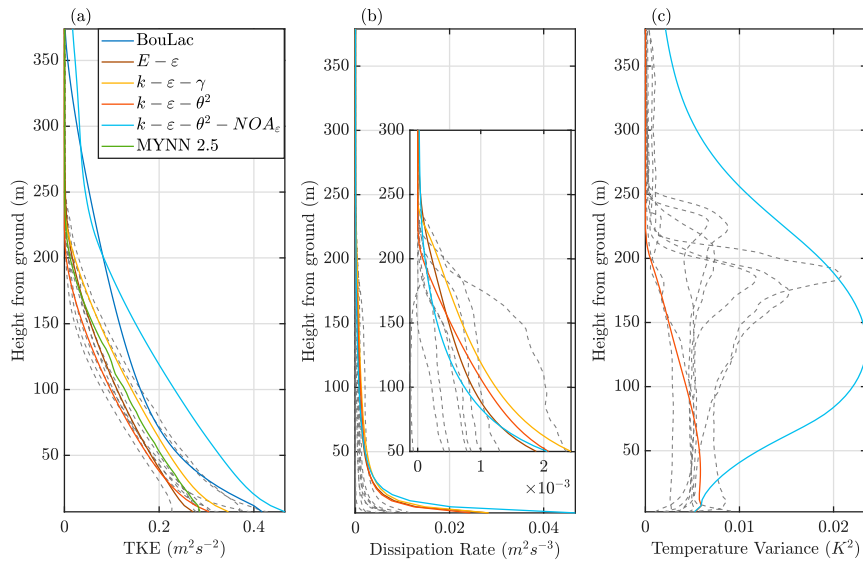
FIG. 16. Vertical profiles of (a) TKE, (b) dissipation rate, and (c) temperature variance for the GABLS case. The series of dashed gray lines refers to the different LES, while color lines refer to the RANS simulations.

Regarding the along-valley wind, K–ε–θ^2 reveals to be the best for the points close to the ridge, where also K–ε–γ shows lower RMSEs with respect to the other simulations. Approaching the valley floor, all RANS simulations present similar errors, while above the valley floor, where the influence of the sidewalls is lower, YSU performs better than the others.

c. SBL in flat terrain

Figure 15 displays the vertical profiles of zonal wind speed (left), potential temperature (center), and meridional wind speed (right) for the GABLS case study, averaged between the eighth and ninth hour of simulation. LES, performed with different atmospheric models, show a boundary layer height between 150 and 200 m, as stated in Beare et al. (2006), and predict a low-level jet (in the S–N direction) forced by the Coriolis term, as well as a peak in the zonal wind speed corresponding to the PBL height. The best RANS simulation in reproducing both wind speed and potential temperature is again K–ε–θ^2, which can correctly capture the height of the boundary layer, while K–ε–γ (where γ is zero in stable conditions) slightly overestimates the PBL height. Also YSU overestimates the PBL height, and, in addition, it underestimates the potential temperature gradient in the inversion layer, resulting in smoother peaks for both U and V at the top of the PBL. MYNN2.5 performs similarly to K–ε–θ^2, but it underestimates the magnitude of the low-level jet. E–ε performs similarly to YSU for all variables, slightly overestimating the PBL height and underestimating the strength of the inversion layer. On the other hand, BouLac fails in reproducing all the vertical profiles, since it does not capture the correct shape of the potential temperature profile and, as a consequence, wrongly estimates the PBL height (~120 m) and overestimates the inversion layer height (~360 m, while it should be ~200 m). The lack of BouLac in correctly

representing the vertical profiles in this specific stable regime is probably due to the wrong calculation of the correct length scale, which strongly depends on the atmospheric stability (see Bougeault and Lacarrere 1989 for further details). Similarly, K–ε–θ^2–NOA$_\varepsilon$, which does not include the additional term in the dissipation rate equation [Eq. (10)], largely overestimates the PBL height (~250 m), and overestimates also the height of the inversion layer, with even larger errors than in BouLac for the wind, while for potential temperature it performs similarly to the other RANS. This overestimation underlines the importance of the additional term A_ε for the dissipation rate equation, which depends linearly on N and on ε itself, increases
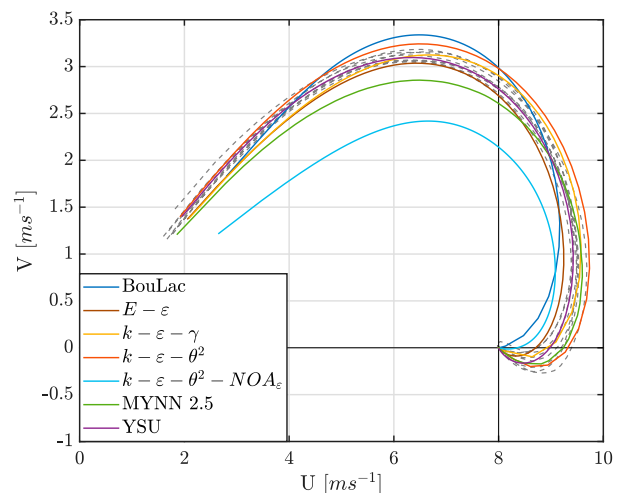

FIG. 17. Hodographs of the mean velocity vector for the GABLS case. The series of dashed black lines refers to the different LES, while color lines refer to the RANS simulations.
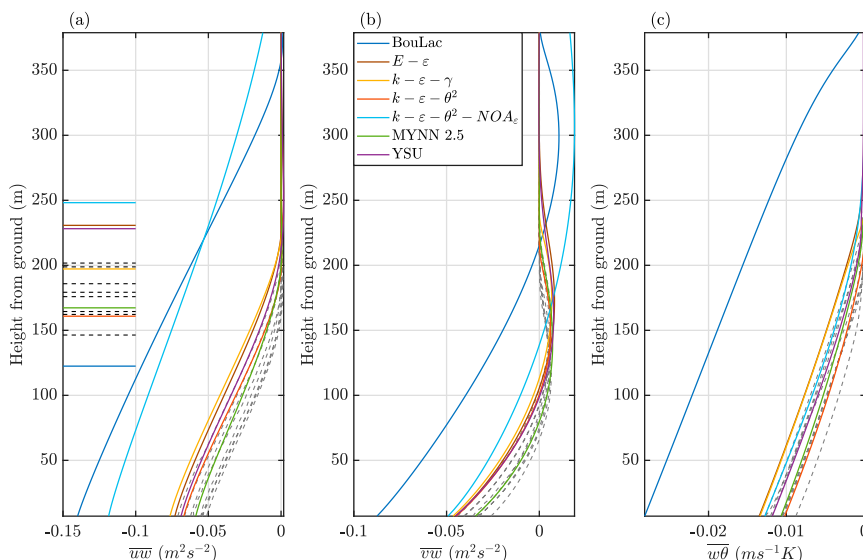
FIG. 18. Vertical profiles of (a) vertical zonal momentum flux, (b) vertical meridional momentum flux(c) and vertical heat flux for the GABLS case. The horizontal lines on the left of (a) show the diagnostic boundary layer height for the RANS simulations and the LES. The series of dashed gray lines refers to the different LES, while color lines refer to the RANS simulations.

the dissipation rate where N is higher (i.e., between 100 and 250 m), hence reducing the PBL height and showing a better agreement with the LES. Indeed, as shown in Fig. 16 (left panel), the TKE of K–ε–θ^2–NOA_ε is highly overestimated, while the TKE of K–ε–θ^2 and K–ε–γ lays always in the range of the different LES. The reduction of the TKE is due to the increase of the dissipation rate in the higher levels (center panel). Since the eddy viscosity and diffusivity are inversely proportional to the dissipation rate, an increase in ε corresponds to a decrease of ν_M and ν_H, and hence in a decrease of TKE, heat and momentum flux. These results confirm that the inclusion of A_ε allows a better representation of the turbulent variables, even considering the temperature variance (right panel of Fig. 16). The $\overline{\theta^2}$ evaluated by the LES assumes a quasi-constant value, with a peak around the PBL height, with different magnitudes for the different simulations. While the temperature variance reproduced by K–ε–θ^2 agrees in terms of shape and magnitude with the various LES, the temperature variance computed by K–ε–θ^2–NOA_ε is largely overestimated, since its computation is linearly dependent on TKE and inversely proportional to ε [see Eq. (13)].

Figure 17 displays the wind odographs from the different simulations. All the simulations, apart from K–ε–θ^2–NOA_ε (which fails throughout the whole vertical air column), well capture the intensity and the direction of the wind speed in the surface layer. At the peak of the low-level jet (where $V \sim 3$ m s^{-1} and $U \sim 6.5$ m s^{-1}), MYNN 2.5 underestimates, while BouLac and K–ε–θ^2 slightly overestimate the low-level jet intensity. Above the low-level jet peak, all the RANS simulations behave well returning to geostrophic conditions, while the two failing in capturing the PBL height (BouLac and K–ε–θ^2–NOA_ε), reach the geostrophic conditions at higher levels.

Figure 18 shows the vertical profiles of zonal momentum flux (left), meridional momentum flux (center) and heat flux (right). While BouLac and K–ε–θ^2–NOA_ε largely overestimate the absolute value of the momentum fluxes, due to an overestimation of the turbulent production (Fig. 16a), the other RANS simulations reasonably reproduce the vertical profile of the fluxes. In particular, the surface heat flux $\overline{w\theta}_s$ is well reproduced by the set of RANS simulations that correctly capture the PBL height. K–ε–γ and E–ε slightly overestimate (in absolute values) all the vertical fluxes and in particular the turbulent heat flux, underlying the importance of adopting a prognostic equation for the temperature variance in both unstable and stable regimes, as pointed out by Zilitinkevich et al. (2007).

5. Summary and conclusions

As the demand for more accurate NWP models increases, especially for complex and heterogeneous terrain, the development of more precise and local turbulence closures is required. To this end, a novel one-dimensional 1.5-order parameterization scheme has been developed, based on the coupled equations for TKE and ε, and included in the WRF Model, with the aim to implement a RANS turbulence closure independent from any length scale. The standard K–ε turbulence scheme has been improved by calculating the turbulent Prandtl number (similarly to Hong et al. 2006) the prognostic equation for temperature variance (Lazeroms et al. 2016), and including an additional term to better reproduce the dissipation rate in stable regimes (Zeng et al. 2020).

Since NWP models are adopted in all areas worldwide, particular attention is paid to the numerical method adopted to solve this set of equations, to obtain the most stable numerical integration that can work at time steps suitable for forecasting

applications. With this goal in mind, an analytical solution for the TKE and ε equations is derived. In this way, the numerical solution is stable and can work with large time steps.

The new turbulence closure is tested in various idealized case studies, under different atmospheric stability and terrain complexity conditions. Tests include the convective boundary layer in flat terrain, the convective thermal circulation induced by a valley, and the well-known GABLS case for the very stable boundary layer. For each test case, our K–ε parameterizations (in two different forms, differing in the parameterization adopted for the counter-gradient term) have been tested against an ensemble of LES, differing in the initial temperature perturbation, and against state-of-the-art RANS turbulence schemes at the first order (YSU), or depending on various diagnostic length scales (BouLac and MYNN2.5).

Results show that in general the novel K–ε scheme always outperforms the other parameterizations, for both wind speed and potential temperature, in all the cases considered in this work. In particular, the largest improvements are found in connection with inversion layers, where the gradients of the mean variables are stronger. The improvement of model performance increases with the increasing complexity of the atmospheric conditions, as for the valley cases, where the enhancements are substantial.

The comparison between the various K–ε closures, differing in the calculation of the counter-gradient term for the turbulent heat flux, underlines the importance of adopting a prognostic equation for the temperature variance $\overline{\theta^2}$. Improvements thanks to the inclusion of the prognostic equation for the temperature variance are evident both in the valley and GABLS cases. Furthermore, the GABLS case confirms that the standard K–ε without the additional production term in the prognostic equation for the dissipation rate is unsuitable for stable boundary layers, and therefore this term is needed for a coherent reproduction of the flow. As pointed out by Zhang et al. (2020), the calculation of the dissipation rate is important for many fields, especially for aviation applications (as in Muñoz-Esparza et al. (2018), where the dissipation rate is calculated diagnostically). The proposed PBL scheme brings substantial improvements even in comparison with a standard E–ε closure, recently implemented in the WRF Model (Zhang et al. 2020). The main differences between our K–ε scheme and the previous one include the surface boundary conditions, the parameterization of the Prandtl number, the calculation of the counter-gradient term for the turbulent heat flux and the model constants, revealing its better performance in all the idealized cases analyzed in this work.

Finally, this work proves that the new scheme discussed here can improve the reproduction of the atmospheric motion in several conditions, going beyond the definition of a diagnostic turbulent length scale commonly adopted in state-of-the-art PBL closures. Future developments will include the validation of the current model in real conditions, through the comparison with observational data, and its coupling with multilayer urban canopy parameterization schemes, in the context of the WRF Model, in order to improve the representation of the complex boundary layer developing over urban areas. Moreover, we aim to extend the here-presented 1D turbulence

closure including the horizontal Reynolds stresses, similarly to Juliano et al. (2022), who presented a 3D version of the Mellor and Yamada (1982) turbulence scheme. This effort is expected to improve the performance of NWP models especially over complex terrain, where the horizontal gradients of the turbulent fluxes can be significant, as highlighted by Goger et al. (2018, 2019).

Data availability statement. Simulations output (LES and RANS) can be provided by the author upon request, as well as the WRF version including the K–ε turbulence closure. LES of the GABLS case study can be found at https://gabls. metoffice.com/lem_data.html.

REFERENCES

Angevine, W. M., H. Jiang, and T. Mauritsen, 2010: Performance of an eddy diffusivity-mass flux scheme for shallow cumulus boundary layers. *Mon. Wea. Rev.*, **138**, 2895–2912, https://doi. org/10.1175/2010MWR3142.1.

Beare, R. J., and Coauthors, 2006: An intercomparison of large-eddy simulations of the stable boundary layer. *Bound.-Layer Meteor.*, **118**, 247–272, https://doi.org/10.1007/s10546-004-2820-6.

Beljaars, A. C. M., J. L. Walmsley, and P. A. Taylor, 1987: A mixed spectral finite-difference model for neutrally stratified boundary-layer flow over roughness changes and topography. *Bound.-Layer Meteor.*, **38**, 273–303, https://doi.org/10.1007/ BF00122448.

Bougeault, P., and P. Lacarrere, 1989: Parameterization of orography-induced turbulence in a mesobeta-scale model. *Mon. Wea. Rev.*, **117**, 1872–1890, https://doi.org/10.1175/1520-0493 (1989)117<1872:POOITI>2.0.CO;2.

Ching, J., R. Rotunno, M. LeMone, A. Martilli, B. Kosovic, P. A. Jimenez, and J. Dudhia, 2014: Convectively induced secondary circulations in fine-grid mesoscale numerical weather prediction models. *Mon. Wea. Rev.*, **142**, 3284–3302, https://doi.org/10.1175/ MWR-D-13-00318.1.

Chrobok, G., S. Raasch, and D. Etling, 1992: A comparison of local and non-local turbulence closure methods for the case of a cold air outbreak. *Bound.-Layer Meteor.*, **58**, 69–90, https://doi.org/10.1007/BF00120752.

Cohen, A. E., S. M. Cavallo, M. C. Coniglio, and H. E. Brooks, 2015: A review of planetary boundary layer parameterization schemes and their sensitivity in simulating southeastern U.S. cold season severe weather environments. *Wea. Forecasting*, **30**, 591–612, https://doi.org/10.1175/WAF-D-14-00105.1.

Craft, T., N. Ince, and B. Launder, 1996: Recent developments in second-moment closure for buoyancy-affected flows. *Dyn. Atmos. Oceans*, **23**, 99–114, https://doi.org/10.1016/0377-0265 (95)00424-6.

Cuxart, J., and Coauthors, 2006: Single-column model intercomparison for a stably stratified atmospheric boundary layer.

Bound.-Layer Meteor., **118**, 273–303, https://doi.org/10.1007/s10546-005-3780-1.

Deardorff, J. W., 1966: The counter-gradient heat flux in the lower atmosphere and in the laboratory. J. Atmos. Sci., **23**, 503–506, https://doi.org/10.1175/1520-0469(1966)023<0503:TCGHFI>2.0.CO;2.

——, 1980: Stratocumulus-capped mixed layers derived from a three-dimensional model. Bound.-Layer Meteor., **18**, 495–527, https://doi.org/10.1007/BF00119502.

Detering, H. W., and D. Etling, 1985: Application of the E–ε turbulence model to the atmospheric boundary layer. Bound.-Layer Meteor., **33**, 113–133, https://doi.org/10.1007/BF00123386.

Duynkerke, P. G., 1988: Application of the E–ϵ turbulence closure model to the neutral and stable atmospheric boundary layer. J. Atmos. Sci., **45**, 865–880, https://doi.org/10.1175/1520-0469(1988)045<0865:AOTTCM>2.0.CO;2.

Giovannini, L., L. Laiti, S. Serafin, and D. Zardi, 2017: The thermally driven diurnal wind system of the Adige Valley in the Italian Alps. Quart. J. Roy. Meteor. Soc., **143**, 2389–2402, https://doi.org/10.1002/qj.3092.

Goger, B., M. W. Rotach, A. Gohm, O. Fuhrer, I. Stiperski, and A. A. Holtslag, 2018: The impact of three-dimensional effects on the simulation of turbulence kinetic energy in a major Alpine Valley. Bound.-Layer Meteor., **168**, 1–27, https://doi.org/10.1007/s10546-018-0341-y.

——, ——, I. Stiperski, O. Fuhrer, and G. de Morsier, 2019: A new horizontal length scale for a three-dimensional turbulence parameterization in mesoscale atmospheric modeling over highly complex terrain. J. Appl. Meteor. Climatol., **58**, 2087–2102, https://doi.org/10.1175/JAMC-D-18-0328.1.

Han, J., M. L. Witek, J. Teixeira, R. Sun, H.-L. Pan, J. K. Fletcher, and C. S. Bretherton, 2016: Implementation in the NCEP GFS of a hybrid eddy-diffusivity mass-flux (EDMF) boundary layer parameterization with dissipative heating and modified stable boundary layer mixing. Wea. Forecasting, **31**, 341–352, https://doi.org/10.1175/WAF-D-15-0053.1.

Hartogensis, O. K., and H. A. R. De Bruin, 2005: Monin–Obukhov similarity functions of the structure parameter of temperature and turbulent kinetic energy dissipation rate in the stable boundary layer. Bound.-Layer Meteor., **116**, 253–276, https://doi.org/10.1007/s10546-004-2817-1.

Hong, S.-Y., Y. Noh, and J. Dudhia, 2006: A new vertical diffusion package with an explicit treatment of entrainment processes. Mon. Wea. Rev., **134**, 2318–2341, https://doi.org/10.1175/MWR3199.1.

Juliano, T. W., B. Kosović, P. A. Jiménez, M. Eghdami, S. E. Haupt, and A. Martilli, 2022: "Gray zone" simulations using a three-dimensional planetary boundary layer parameterization in the Weather Research and Forecasting Model. Mon. Wea. Rev., **150**, 1585–1619, https://doi.org/10.1175/MWR-D-21-0164.1.

Kosović, B., and J. A. Curry, 2000: A large eddy simulation study of a quasi-steady, stably stratified atmospheric boundary layer. J. Atmos. Sci., **57**, 1052–1068, https://doi.org/10.1175/1520-0469(2000)057<1052:ALESSO>2.0.CO;2.

Langland, R. H., and C.-S. Liou, 1996: Implementation of an E–ϵ parameterization of vertical subgrid-scale mixing in a regional model. Mon. Wea. Rev., **124**, 905–918, https://doi.org/10.1175/1520-0493(1996)124<0905:IOAPOV>2.0.CO;2.

Launder, B., and D. Spalding, 1974: The numerical computation of turbulent flows. Comput. Methods Appl. Mech. Eng., **3**, 269–289, https://doi.org/10.1016/0045-7825(74)90029-2.

——, and ——, 1983: The numerical computation of turbulent flows. Numerical Prediction of Flow, Heat Transfer, Turbulence and Combustion: Selected Works of Professor D. Brian Spalding, S. V. Patankar et al., Eds., Elsevier, 96–116.

Lazeroms, W. M. J., G. Brethouwer, S. Wallin, and A. Johansson, 2015: Efficient treatment of the nonlinear features in algebraic Reynolds-stress and heat-flux models for stratified and convective flows. Int. J. Heat Fluid Flow, **53**, 15–28, https://doi.org/10.1016/j.ijheatfluidflow.2015.01.005.

——, G. Svensson, E. Bazile, G. Brethouwer, S. Wallin, and A. V. Johansson, 2016: Study of transitions in the atmospheric boundary layer using explicit algebraic turbulence models. Bound.-Layer Meteor., **161**, 19–47, https://doi.org/10.1007/s10546-016-0194-1.

Lee, W., 2011: Tridiagonal matrices: Thomas algorithm. Scientific Computation MS6021, University of Limerick, 3 pp., http://www.industrial-maths.com/ms6021_thomas.pdf.

Lew, A. J., G. C. Buscaglia, and P. M. Carrica, 2001: A note on the numerical treatment of the k–ϵ turbulence model. Int. J. Comput. Fluid Dyn., **14**, 201–209, https://doi.org/10.1080/10618560108940724.

Mauritsen, T., G. Svensson, S. S. Zilitinkevich, I. Esau, L. Enger, and B. Grisogono, 2007: A total turbulent energy closure model for neutrally and stably stratified atmospheric boundary layers. J. Atmos. Sci., **64**, 4113–4126, https://doi.org/10.1175/2007JAS2294.1.

Mellor, G. L., and T. Yamada, 1982: Development of a turbulence closure model for geophysical fluid problems. Rev. Geophys., **20**, 851, https://doi.org/10.1029/RG020i004p00851.

Moeng, C.-H., J. Dudhia, J. Klemp, and P. Sullivan, 2007: Examining two-way grid nesting for large eddy simulation of the PBL using the WRF Model. Mon. Wea. Rev., **135**, 2295–2311, https://doi.org/10.1175/MWR3406.1.

Monin, A. S., and A. M. Obukhov, 1954: Basic laws of turbulent mixing in the surface layer of the atmosphere. Tr. Akad. Nauk SSSR Geophiz. Inst., **24**, 163–187.

Muñoz-Esparza, D., R. D. Sharman, and J. K. Lundquist, 2018: Turbulence dissipation rate in the atmospheric boundary layer: Observations and WRF mesoscale modeling during the XPIA field campaign. Mon. Wea. Rev., **146**, 351–371, https://doi.org/10.1175/MWR-D-17-0186.1.

Nakanishi, M., and H. Niino, 2004: An improved Mellor–Yamada level-3 model with condensation physics: Its design and verification. Bound.-Layer Meteor., **112**, 1–31, https://doi.org/10.1023/B:BOUN.0000020164.04146.98.

Nielsen-Gammon, J. W., and Coauthors, 2008: Multisensor estimation of mixing heights over a coastal city. J. Appl. Meteor. Climatol., **47**, 27–43, https://doi.org/10.1175/2007JAMC1503.1.

——, X. M. Hu, F. Zhang, and J. E. Pleim, 2010: Evaluation of planetary boundary layer scheme sensitivities for the purpose of parameter estimation. Mon. Wea. Rev., **138**, 3400–3417, https://doi.org/10.1175/2010MWR3292.1.

Olson, J. B., J. S. Kenyon, W. A. Angevine, J. M. Brown, M. Pagowski, and K. Sušelj, 2019: A description of the MYNN-EDMF scheme and the coupling to other components in WRF-ARW. NOAA Tech. Memo. OAR GSD-61, 42 pp., https://doi.org/10.25923/n9wm-be49.

Park, S. H., J. B. Klemp, and J. H. Kim, 2019: Hybrid mass coordinate in WRF-ARW and its impact on upper-level turbulence forecasting. Mon. Wea. Rev., **147**, 971–985, https://doi.org/10.1175/MWR-D-18-0334.1.

Rampanelli, G., D. Zardi, and R. Rotunno, 2004: Mechanisms of up-valley winds. J. Atmos. Sci., **61**, 3097–3111, https://doi.org/10.1175/JAS-3354.1.

Schmidli, J., and Coauthors, 2011: Intercomparison of mesoscale model simulations of the daytime valley wind system. *Mon. Wea. Rev.*, **139**, 1389–1409, https://doi.org/10.1175/2010MWR3523.1.

Serafin, S., and D. Zardi, 2010: Structure of the atmospheric boundary layer in the vicinity of a developing upslope flow system: A numerical model study. *J. Atmos. Sci.*, **67**, 1171–1185, https://doi.org/10.1175/2009JAS3231.1.

Shih, T.-H., W. W. Liou, A. Shabbir, Z. Yang, and J. Zhu, 1995: A new $k - \varepsilon$ eddy viscosity model for high Reynolds number turbulent flows. *Comput. Fluids*, **24**, 227–238, https://doi.org/10.1016/0045-7930(94)00032-T.

Skamarock, W., and Coauthors, 2019: A description of the Advanced Research WRF Model version 4. NCAR Tech. Note NCAR/TN-556+STR, 145 pp., https://doi.org/10.5065/1dfh-6p97.

Souma, K., and Y. Wang, 2009: Improved simulation of the East Asian summer monsoon rainfall with satellite-derived snow water equivalent data. *Mon. Wea. Rev.*, **137**, 1790–1804, https://doi.org/10.1175/2008MWR2800.1.

Stull, R. B., Ed., 1988: *An Introduction to Boundary Layer Meteorology*. Kluwer Academic, 666 pp.

Sukoriansky, S., B. Galperin, and V. Perov, 2005: Application of a new spectral theory of stably stratified turbulence to the atmospheric boundary layer over sea ice. *Bound.-Layer Meteor.*, **117**, 231–257, https://doi.org/10.1007/s10546-004-6848-4.

Troen, I. B., and L. Mahrt, 1986: A simple model of the atmospheric boundary layer; sensitivity to surface evaporation. *Bound.-Layer Meteor.*, **37**, 129–148, https://doi.org/10.1007/BF00122760.

van der Laan, M. P., M. C. Kelly, and N. N. Sørensen, 2017: A new k–epsilon model consistent with Monin–Obukhov similarity theory. *Wind Energy*, **20**, 479–489, https://doi.org/10.1002/we.2017.

Wagner, J. S., A. Gohm, and M. W. Rotach, 2014: The impact of horizontal model grid resolution on the boundary layer structure over an idealized valley. *Mon. Wea. Rev.*, **142**, 3446–3465, https://doi.org/10.1175/MWR-D-14-00002.1.

Wang, Y., 2001: An explicit simulation of tropical cyclones with a triply nested movable mesh primitive equation model: TCM3. Part I: Model description and control experiment. *Mon. Wea. Rev.*, **129**, 1370–1394, https://doi.org/10.1175/1520-0493(2002)130<3022:AESOTC>2.0.CO;2.

——, 2002: An explicit simulation of tropical cyclones with a triply nested movable mesh primitive equation model: TCM3. Part II: Model refinements and sensitivity to cloud microphysics parameterization. *Mon. Wea. Rev.*, **130**, 3022–3036, https://doi.org/10.1175/1520-0493(2002)130<3022:AESOTC>2.0.CO;2.

——, O. L. Sen, and B. Wang, 2003: A highly resolved regional climate model (IPRC-RegCM) and its simulation of the 1998 severe precipitation event over China. Part I: Model description and verification of simulation. *J. Climate*, **16**, 1721–1738, https://doi.org/10.1175/1520-0442(2003)016<1721:AHRRCM>2.0.CO;2.

——, S.-P. Xie, H. Xu, and B. Wang, 2004a: Regional model simulations of marine boundary layer clouds over the Southeast Pacific off South America. Part I: Control experiment. *Mon. Wea. Rev.*, **132**, 274–296, https://doi.org/10.1175/1520-0493(2004)132<0274:RMSOMB>2.0.CO;2.

——, H. Xu, and S.-P. Xie, 2004b: Regional model simulations of marine boundary layer clouds over the Southeast Pacific off South America. Part II: Sensitivity experiments. *Mon. Wea. Rev.*, **132**, 2650–2668, https://doi.org/10.1175/MWR2812.1.

Willis, G. E., and J. W. Deardorff, 1974: A laboratory model of the unstable planetary boundary layer. *J. Atmos. Sci.*, **31**, 1297–1307, https://doi.org/10.1175/1520-0469(1974)031<1297:ALMOTU>2.0.CO;2.

Xie, S.-P., and Coauthors, 2007: A regional ocean–atmosphere model for eastern Pacific climate: Toward reducing tropical biases. *J. Climate*, **20**, 1504–1522, https://doi.org/10.1175/JCLI4080.1.

Želi, V., G. Brethouwer, S. Wallin, and A. V. Johansson, 2019: Consistent boundary-condition treatment for computation of the atmospheric boundary layer using the explicit algebraic Reynolds-stress model. *Bound.-Layer Meteor.*, **171**, 53–77, https://doi.org/10.1007/s10546-018-0415-x.

Zeng, X., and Y. Wang, 2020: A k–ϵ turbulence model for the convective atmosphere. *J. Atmos. Sci.*, **77**, 3891–3906, https://doi.org/10.1175/JAS-D-20-0072.1.

——, ——, and B. T. MacCall, 2020: A k–ϵ turbulence model for the stable atmosphere. *J. Atmos. Sci.*, **77**, 167–184, https://doi.org/10.1175/JAS-D-19-0085.1.

Zhang, C., Y. Wang, and M. Xue, 2020: Evaluation of an E– and three other boundary layer parameterization schemes in the WRF Model over the southeast Pacific and the Southern Great Plains. *Mon. Wea. Rev.*, **148**, 1121–1145, https://doi.org/10.1175/MWR-D-19-0084.1.

Zhang, X., J. W. Bao, B. Chen, and E. D. Grell, 2018: A three-dimensional scale-adaptive turbulent kinetic energy scheme in the WRF-ARW Model. *Mon. Wea. Rev.*, **146**, 2023–2045, https://doi.org/10.1175/MWR-D-17-0356.1.

Zilitinkevich, S. S., T. Elperin, N. Kleeorin, and I. Rogachevskii, 2007: Energy- and Flux-Budget (EFB) turbulence closure model for stably stratified flows. Part I: Steady-state, homogeneous regimes. *Bound.-Layer Meteor.*, **125**, 167–191, https://doi.org/10.1007/s10546-007-9189-2.

——, ——, ——, ——, and I. Esau, 2013: A hierarchy of Energy- and Flux-Budget (EFB) turbulence closure models for stably-stratified geophysical flows. *Bound.-Layer Meteor.*, **146**, 341–373, https://doi.org/10.1007/s10546-012-9768-8.